PHYSICAL REVIEW A, VOLUME 62, 023401

Tunneling through light-induced molecular potentials in $Ar_2{}^+$

Christof Wunderlich,[1,]* Hartmut Figger,[2] and Theodor W. Hänsch[2]
[1]*Institut für Laser-Physik, Universität Hamburg, Jungiusstraße 9, D-20355 Hamburg, Germany*
[2]*Max-Planck-Institut für Quantenoptik, D-85748 Garching, Germany*

(Received 16 December 1999; published 13 July 2000)

A photodissociation study is reported on the simply structured molecular ion $Ar_2{}^+$ that is, to good approximation a two-electronic state system (one bound, the other dissociative) under the conditions of this experiment. Nonlinear behavior is manifest in characteristically changed dissociation dynamics as a function of laser intensity in strong laser fields ($\leqslant 5\times10^{12}$ W/cm^2). Light-induced molecular potentials (molecular dressed states) provide a convenient description under such conditions and predict surprising effects regarding molecular dynamics in a light field. Much care has been taken to assure a meaningful quantitative comparison of experimental results with numerical simulations. This leads to the identification of dissociation by tunneling through a light-induced molecular potential well. $Ar_2{}^+$ is generated in a dc-discharge, accelerated, and formed into a mass selected molecular beam (7.5 keV). For some experiments, molecules are prepared in low vibrational states only, before they interact with a high intensity laser beam at a wavelength of 532 nm. The momentum distribution of photofragments is measured using an imaging technique for neutral fragments.

PACS number(s): 42.50.Hz, 33.80.−b, 33.80.Gj, 42.50.Ct

I. INTRODUCTION

Studying the response of matter to intense light fields has brought about a wealth of new phenomena in atoms and molecules [1,2]. The nonlinear response of molecules to strong fields leads to various new effects that might be exploited to control intramolecular and intermolecular dynamics. Inherent possibilities of light-induced molecular potentials created by an intense laser field for the manipulation of chemical reactions have been recognized in the 1970's [3] when the dressed state formalism, originally developed for atoms [4], was applied to describe the molecule-light interaction. Making use of this intuitive physical model, photodissociation of $Ar_2{}^+$ was theoretically investigated and, for instance, stabilization against photodissociation in intense fields predicted [5,6]. Exploiting features of light-induced potentials, isotope separation by photodissociation of $H_2{}^+$ and D_2^+ [7], and coherent control of the photodissociation of $H_2{}^+$ using two strong laser fields has been proposed (for instance, Ref. [8]) and experimentally observed [9]. A further example for the use of intense light fields to control molecular dynamics is the altered reaction dynamics of proton exchange between H and H_2. This has been suggested to be feasible, for instance, in Ref. [10]. A scheme for adiabatic transfer of wave packets between molecular electronic states by propagating them on light-induced potentials is presented in a recent theoretical study [11].

In order to gain fundamental understanding of individual phenomena in intense fields as, for example, nonlinear photoionization or photodissociation, it is advantageous to reduce the number of degrees of freedom by first studying diatomic molecules. Even in diatomics a rich electronic structure might be an impediment when trying to observe different nonlinear effects separately. In order to first better understand and then to use that knowledge to eventually control nonlinear behavior in, for example, photodissociation, choosing the simplest of all molecules, $H_2{}^+$, is a reasonable choice: it possesses a bound electronic ground state, $^2\Sigma_g^+$ while the first excited state, $^2\Sigma_u^+$ is repulsive. Other excited states are energetically far away from these two lowest states.

Numerous theoretical and experimental studies have helped to elucidate the complicated dynamics of molecules in intense laser fields and, in particular, of their simplest representatives $H_2{}^+$ and H_2. Theoretical investigations of this prototype molecule have predicted, in addition to the work cited above, for instance, efficient generation of harmonics [12], and stabilization against dissociation in intense laser fields (for instance, Refs. [13,14]). The experimental verification of the latter effect using H_2 [15], Cl_2 [16], and I_2 [17] molecules remains controversial. Enhanced ionization at a certain range of internuclear separation is predicted, for instance, in Refs. [18] and experimental evidence has been obtained from investigations of I_2 [19,17], and recently of H_2 in intense fields [20]. Further recent theoretical work on molecules in intense fields, and in particular on H_2 and $H_2{}^+$ includes Refs. [21]. More experiments on H_2 are reported, for instance, in Refs. [22,23], whereas experimental work on molecules other than H_2 can be found, for instance, in Ref. [24].

On the experimental side, almost all investigations have concentrated on neutral molecules. Several experimental studies of intense field dissociation and ionization have used neutral H_2 as a starting point that is ionized and dissociated by one laser pulse. This makes the interpretation of photoelectron and photofragment spectra in terms of a specific ionization and/or dissociation channel of the molecular *ion* not always unambiguous. Recently, molecular beam experiments have been carried out that use directly the molecular ions $Ar_2{}^+$ and $H_2{}^+$ as a starting point for studies of their behavior in intense fields [25–28].

Nonlinear effects that occur when coupling any two elec-

---

*Email address: wunderlich@physnet.uni-hamburg.de tronic states by intense laser light (both of them may also be bound states) are expected to become appreciable when the laser-induced electronic Rabi-frequency $\omega_{\text{Rabi}}=\vec{D}\cdot\vec{\mathcal{E}}/\hbar$ is comparable to or larger than the vibrational frequency ω_e of the nuclei ($\vec{\mathcal{E}}$ is the applied electric field, and $\vec{D}$ the electronic transition dipole moment) [29]. Thus, to induce appreciable nonlinear behavior, it is advantageous to choose a molecule with small ω_e and large induced dipole moment D between electronic states. The notion ''intense field,'' therefore, is to be seen in relation to the molecular states the field $\mathcal{E}\propto\sqrt{I}$ is applied to (I is the intensity of the laser field). With the Rabi frequency being proportional to the square root of the laser intensity, it is clear that the smaller the vibrational frequency, the lower is the required laser intensity to induce nonlinear behavior.

A well suited object for studying two molecular states coupled by an intense field is $\text{Ar}_2{}^+$ [5,30,31] that possesses, similar to $\text{H}_2{}^+$, a bound and a repulsive electronic state. The lowest bound state, $A\,{}^2\Sigma_u^+$ of $\text{Ar}_2{}^+$ is characterized by a vibrational frequency about an order of magnitude smaller than that of $\text{H}_2{}^+$, and is coupled via a strong transition dipole moment (roughly equal to $r/2$ a.u. as in $\text{H}_2{}^+$, where r denotes the internuclear separation) to the repulsive $D\,{}^2\Sigma_g^+$ state. The light-induced Rabi frequency ω_{Rabi} is approximately equal to ω_e already at the relatively moderate intensity of 10^{10} W/cm^2. Therefore, one may work in an intensity regime where the rate of ionization is still negligible when using short laser pulses, which greatly facilitates the interpretation of experimental results. The experiments presented here investigate how, by inducing a transition moment between a bound and a repulsive state in $\text{Ar}_2{}^+$, photodissociation dynamics is modified in a characteristic way in intense fields.

When using light-induced molecular potentials (molecular dressed states [29]) as a tool to interpret molecular dynamics in laser fields, modifications of the dynamics due to nonlinear processes are conveniently visualized. Qualitative behavior of molecules in intense fields can be predicted without having to resort to sophisticated calculations. Quantitative predictions are feasible even for realistic experimental situations where, for example, averaging over a large range of intensities, pulse lengths, and population distributions over molecular states is necessary. Other methods would often require prohibitive computing power under these conditions.

In this publication we show how a quantitative interpretation of results of photofragment spectroscopy on the simply structured molecular ion $\text{Ar}_2{}^+$ prepared in a mass selected molecular beam leads to the clear identification of a particular effect of light-induced molecular potentials: tunneling through a light-induced potential barrier. The experimental observation of this nonlinear effect has been described first in Ref. [26] and here we present a detailed account thereof including new evidence that corroborates the conclusions drawn from experimental data. We shall emphasize that in many cases a *quantitative* comparison between theory and experiment in photofragment spectroscopy is necessary to identify effects of light-induced potentials (LIPs).

II. PHOTODISSOCIATION OF $\text{Ar}_2{}^+$: THEORY

Dissociation of $\text{Ar}_2{}^+$ after net absorption of one photon will be considered in what follows. First the relevant bound-free transition in $\text{Ar}_2{}^+$ is described using the usual treatment at low laser intensity: Fermi's golden rule (FGR). Then, nonlinear effects appearing at higher intensity as deviations from predictions of FGR will be investigated using the concept of light induced potentials. This leads not only to an intuitive qualitative understanding, but also yields a good quantitative description of nonlinear photodissociation of $\text{Ar}_2{}^+$ in intense laser fields.

A. Fermi's golden rule

The four lowest electronic states of $\text{Ar}_2{}^+$ correlating with the atomic ground states of Ar and Ar^+ are labeled $A\,{}^2\Sigma_u^+$, $B\,{}^2\Pi_g$, $C\,{}^2\Pi_u$, and $D\,{}^2\Sigma_g^+$ in ascending energetic order [32]. When irradiating molecules in the electronic ground state $A\,{}^2\Sigma_u^+$ with laser light in the wavelength range from 480 to 555 nm (as is used in these investigations), transitions to other states than $D\,{}^2\Sigma_g^+$ can be neglected, since the electronic transition moment, $\mu(r)$ in this wavelength range for transitions from $A\,{}^2\Sigma_u^+$ to Π states is at least two orders of magnitude smaller [33] than for the $A\,{}^2\Sigma_u^+-D\,{}^2\Sigma_g^+$ transition. Thus, contributions of Π states to the photodissociation cross-section are negligible. This has been confirmed in our experiments (Sec. IV A and Ref. [34]). Potential curves of the relevant states $A\,{}^2\Sigma_u^+$ and $D\,{}^2\Sigma_g^+$ states have been optimized using results of *ab initio* calculations [33] together with available experimental data [35] and our own measurements. This will be detailed elsewhere [34].

Starting from Fermi's golden rule, the photodissociation cross section $\sigma_{\omega_L,\nu,K}$ (employing light of frequency ω_L) for the $A\,{}^2\Sigma_u^+-D\,{}^2\Sigma_g^+$ transition is given by [36]

$$\sigma_{\omega_L,\nu,K}=4.42\times10^{-17}\frac{2U_D+|U_{\nu,K}|+\Delta U}{\sqrt{2U_D}}|M_{\omega_L,\nu,K}|^2\ \text{cm}^2. \tag{1}$$

The kinetic energy of both photofragments is denoted by $2U_D$, and $U_{\nu,K}$ stands for the binding energy of the level characterized by vibrational quantum number ν and rotational quantum number K. The fine structure splitting in the ground state of Ar^+ is denoted by ΔU, and M is the dipole matrix element between bound and continuum states given by

$$M_{\omega_L,\nu,K}=\int_0^\infty \chi_{\nu,K}(r)\chi_{U_D,K}(r)\mu_\Sigma(r)dr. \tag{2}$$

$\chi_{\nu,K}(r)$ and $\chi_{U_D,K}(r)$ represent the bound and continuum nuclear wave functions, respectively. The electronic dipole moment is denoted by $\mu_\Sigma(r)$ which depends on the internuclear distance r. The nuclear wavefunctions have been evaluated by numerical integration of the Schrödinger equation using the Numerov method (accurate to fifth order in step size $\delta r=0.003a_0$, with a_0 being the Bohr radius). In all cal-

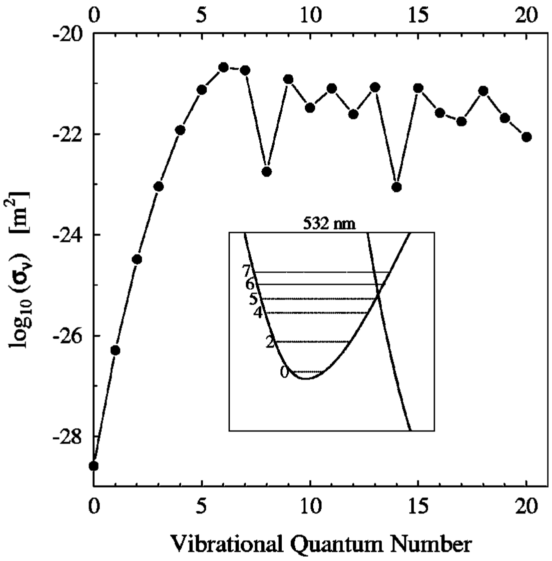

FIG. 1. Cross section for photodissociation of $Ar_2{}^+$ ($A\,{}^2\Sigma_u^+$ - $D\,{}^2\Sigma_g^+$ transition) at laser wavelength 532 nm (rotational quantum number $K=1$). The inset shows diabatic field-electronic states $A\,{}^2\Sigma_u^+ + (n+1)\hbar\omega_L$ and $D\,{}^2\Sigma_g^+ + n\hbar\omega_L$ (compare Sec. II B). Dotted lines indicate diabatic vibrational levels.

culations presented here we have always included the r dependence of the dipole moment in the overlap integral $M_{\omega_L,\nu,K}$.

For fixed laser wavelength the size of the photodissociation cross-section is determined by the Franck-Condon-like factor $M_{\omega_L,\nu,K}$. Figure 1 shows the calculated ν-dependent cross section ($K=1$) at a laser wavelength of 532 nm. The exponential tail of wave functions of low vibrational states of the $A\,{}^2\Sigma_u^+$ state reaches far into the classically forbidden region at large r. For the discussion of experimental findings to follow in the next sections, it is important to note that this produces small but nonzero M factors even for small ν. With increasing ν the overlap between bound and continuum wavefunctions reaches a maximum for $\nu=6$ at 532 nm.

For simulating the experiment, the dissociation rate, R is needed that is related to the cross section σ by

$$R_{\omega_L,\nu,K} = \sigma_{\omega_L,\nu,K}\frac{I}{\hbar\omega_L}, \tag{3}$$

where $\hbar$ is Planck's constant divided by 2π.

B. Light-induced molecular potentials

The Hamiltonian of a molecule can be written as

$$H_{\text{mol}} = T_N(r) + H_e(\{\vec{r}_k\},r), \tag{4}$$

where T_N describes the kinetic energy of the nuclei, H_e contains electrostatic terms and the kinetic energy of the electrons, and $\{\vec{r}_k\}$ stands for the coordinates of the electrons. Separating the motion of electrons and nuclei (Born-Oppenheimer approximation), the electronic eigenvalues and eigenstates of the molecule are calculated from

$$H_e|\varphi_i(\{\vec{r}_k\},r)\rangle = W_i(r)|\varphi_i(\{\vec{r}_k\},r)\rangle, \tag{5}$$

where r appears as a parameter. Here we restrict ourselves to a two-state diatomic molecule with potential curves $W_i(r)$, $i=1,2$.

In a dressed state description of light-molecule interaction the Hamiltonian of the quantized light field

$$H_L|n\rangle = \hbar\omega_L a^\dagger a|n\rangle = \hbar\omega_L\left(n+\frac{1}{2}\right)|n\rangle \tag{6}$$

(n is the photon number in a mode of the monochromatic light field with frequency ω_L, $a^\dagger$ and a are the creation and annihilation operators of the quantized light field) becomes part of the total Hamiltonian

$$H_{tot} = T_N(r) + H_e(\{\vec{r}_k\},r) + H_L + V, \tag{7}$$

where V is the interaction term between light and molecule. Again, we look for solutions of

$$H|\Phi_i^{F+e}(r)\rangle = E_i(r)|\Phi_i^{F+e}(r)\rangle, \quad i=1,2. \tag{8}$$

with $|\Phi_i^{F+e}(r)\rangle$ being field-electronic states and $H \equiv H_{tot} - T_N$.

The interaction term becomes in rotating wave approximation (RWA)

$$V_{\text{RWA}} = g(r)(a\sigma_+ + a^\dagger\sigma_-). \tag{9}$$

Here $\sigma_\pm = \sigma_x \mp \sigma_y$ ($\sigma_{x,y}$ are the Pauli matrices), and $g(r)$ is the coupling constant.

A molecular transition induced by V_{RWA} from W_1 to W_2 (or vice versa) can only occur in connection with the annihilation (creation) of a photon. Consequently, H can be written as a sum of noncoupled Hamiltonians acting on 2×2 sub-Hilbert-spaces $H=\Sigma_n H_n$ with

$$H_n = \begin{pmatrix} W_1(r)+(n+1)\hbar\omega_L & g(r) \\ g(r) & W_2(r)+n\hbar\omega_L \end{pmatrix} \tag{10}$$

For fields containing a large number of photons, for example, a coherent intense field emitted by a laser with $\langle\triangle n\rangle/\langle n\rangle \ll 1$ [4], the dynamics of the molecule-light interaction can be fully described (within the RWA) by considering, for example, $H_{\langle m\rangle}$ with $m \simeq \langle n\rangle$ (m is the closest integer to the real number $\langle n\rangle$). The coupling constant

$$g = \frac{1}{2}|\langle\varphi_1|\vec{D}\cdot\vec{\mathcal{E}}|\varphi_2\rangle|, \tag{11}$$

where $\vec{D}$ is the electric dipole operator and $\vec{\mathcal{E}} = \mathcal{E}\vec{e}$, with electric field strength $\mathcal{E}$ and polarization vector $\vec{e}$.

Diagonalizing H_m gives the field-electronic eigenvalues (light-induced potential curves) $E_i(r)$:

$$E_{1,2}(r) = \frac{1}{2}[W_1(r)+\hbar\omega_L+W_2(r)] \pm \frac{1}{2}\sqrt{\delta^2+\hbar^2\omega_{\text{Rabi}}^2}, \tag{12}$$

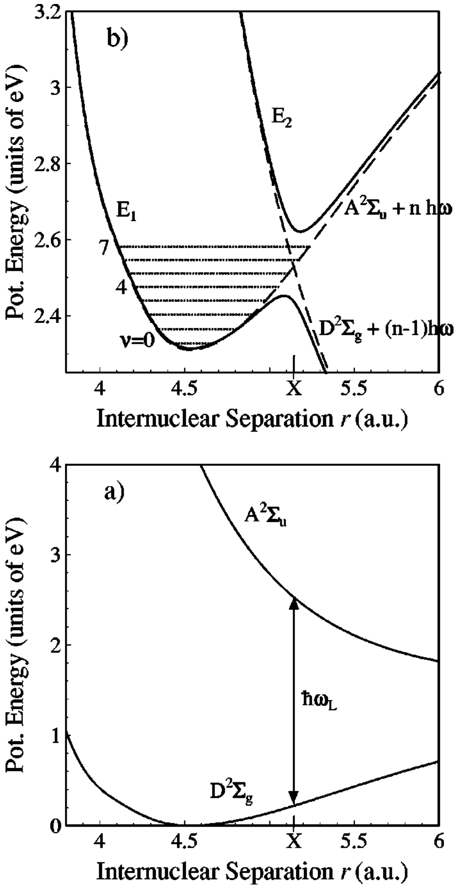

FIG. 2. (a) $A\,^2\Sigma_u^+$ and $D\,^2\Sigma_g^+$ states of $\mathrm{Ar_2}^+$. The coupling of these electronic states by a light field at 532 nm is indicated by the vertical arrow. (b) Light induced molecular potentials E_1 and E_2 (dressed states, shown by solid lines) of $\mathrm{Ar_2}^+$ (532 nm, 5×10^{11} W/cm^2) and diabatic field-electronic states (bare states, dashed lines). Dotted horizontal lines indicate diabatic vibrational levels.

with

$$\delta(r)\equiv W_1(r)+\hbar\omega_L-W_2(r) \tag{13}$$

and

$$\omega_{Rabi}(r)\equiv 2\frac{g(r)}{\hbar}. \tag{14}$$

Diagonal elements of the matrix given in Eq. (10) represent diabatic potential curves in a light field that cross at internuclear distance $r=X$. One obtains these diabatic curves from molecular potentials W_i by shifting the lower of the two potential curves up by the energy $\hbar\omega_L$ of one photon. Dashed lines in Fig. 2 represent these diabatic curves for $\mathrm{Ar_2}^+$, the molecule used in the experiments described here. After diagonalizing matrix 10, the degeneracy at $r=X$ is lifted and two new adiabatic potential curves E_i with an avoided crossing constrain the motion of the nuclei. The change of nuclear dynamics due to the light field can be conveniently visualized as arising from these new light-induced molecular potential curves [26].

Light-induced potentials (LIP) do not only provide a pictorial view of intramolecular nuclear dynamics, but can be used to predict, for example, dissociation rates of $\mathrm{Ar_2}^+$ in intense laser fields by using Landau-Zener type formulas [37,26]. Quantitative results from LIP are expected to be correct in cw fields, and in pulsed field situations where vibrational levels can follow adiabatically the change in shape of LIP due to variation of the laser intensity, i.e., the relative change in intensity $|(dI/dt)/I|$ is much smaller than the inverse of the molecular vibrational period τ. Under this condition LIP are well defined. For shorter laser pulses, they still provide a useful qualitative tool aiding in the interpretation of experimental findings.

The qualitative behavior of the dissociation rate as a function of the vibrational quantum number can be seen by inspection of Fig. 2: vibrational states in the vicinity of the avoided crossing are no longer bound and will dissociate easily, that is, these states will have the largest photodissociation cross sections. This is in accordance with numerical results from FGR (Fig. 1): vibrational states in the region of the avoided potential crossing have a large overlap integral M, whereas low lying states have only small overlap with continuum states of $D\,^2\Sigma_g^+$. Low vibrational states below the barrier of the lower light-induced potential can only dissociate via tunneling. Obviously, this will be easier the smaller the barrier is, that is, with increasing ν, the dissociation cross section for a given intensity will grow, or equivalently, for fixed ν, the dissociation cross section increases with increasing intensity.

C. Comparison of the predictions of LIP and FGR

In Fig. 2 of Ref. [26] the dissociation rates for some vibrational states ($K=1$) calculated from LIP and FGR, respectively are compared. The rates from LIP are calculated for $\theta=0$, $\phi\in[0,2\pi)$ with θ and ϕ being the polar and azimuthal angle, respectively between the axis of laser polarization and the internuclear axis. (The electronic transition moment μ_Σ for the $A\,^2\Sigma_u^+$–$D\,^2\Sigma_g^+$ transition is parallel to the internuclear axis.) The cross sections shown, however, are averaged over solid angle, and, in order to compare the two rates, the rate derived from FGR, therefore, has to be multiplied by a factor 3. For low laser intensity LIP and FGR give the same result for all vibrational states. At high intensity, however, tunneling through the light-induced barrier of E_1 leads to a dramatic increase in the dissociation rate for low vibrational states ($\nu\leqslant3$). When the dissociation probability, P calculated from LIP approaches 1, the rate, P/τ, saturates at $1/\tau$. Levels with $\nu\geqslant5$ are characterized by a large dissociation rate in both pictures, FGR and LIP, and high laser intensity does not lead to a difference in the predicted dissociation yield from these levels [25]. Thus, in order to observe the effect of tunneling experimentally, it is advantageous to have low vibrational states appreciably populated. We do not consider here possible stabilization of levels above the avoided crossing of E_1 and E_2, since this effect is operative only in shorter laser pulses than employed in this study.

For high laser intensity, the tunneling rate grows strongly with increasing laser intensity and the dissociation rate of

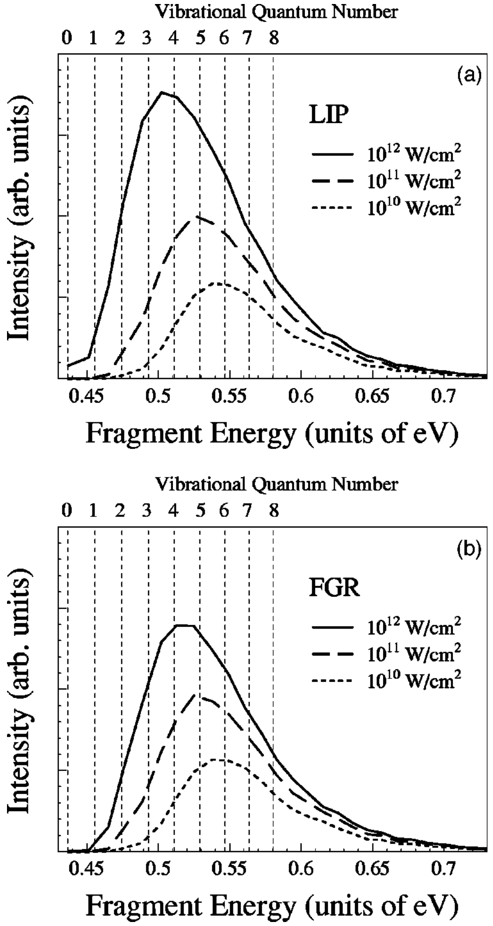

FIG. 3. Calculated kinetic energy spectrum of photofragments originating from the $A\,{}^2\Sigma_u^+ – D\,{}^2\Sigma_g^+$ transition in $\mathrm{Ar_2}^+$ ($kT = 0.068$ eV) for different laser intensities at a wavelength of 532 nm and pulse length 38 ps. (a) Fermi's golden rule. (b) Light-induced potentials.

low ν-states at high intensity surpasses by many orders of magnitude the one predicted by FGR (Fig. 2 [26]). This leads to the appearance of photofragments of low kinetic energy. In order to diagnose this effect of LIP experimentally, it is necessary to monitor *quantitatively* the dissociation rate (or a quantity proportional to it) as a function of intensity, since the appearance of low kinetic energy fragments is predicted by FGR, too: At high intensity (10^{11} W/cm^2, Fig. 3) all higher vibrational levels are excited to the dissociative $D\,{}^2\Sigma_g^+$ state and increasing the intensity even further to 10^{12} W/cm^2 leads to a relative increase in the number of low energy fragments stemming from low ν levels, that is, the kinetic energy spectrum of the fragments is broadened towards smaller energy. The spectra shown in Fig. 3 are obtained by integration over time and solid angle of Eq. (21) using Gaussian laser pulses of 38 ps FWHM at 532 nm and a thermal population distribution of rovibrational states at $kT = 0.068$ eV assuming an energy resolution of 30 meV. Kinetic energies of fragments from different vibrational states (rotational quantum number $K = 1$) are indicated by vertical dashed lines. Such a broadening of kinetic energy spectra towards small energies is also observed when the interaction time between light and molecules is increased at some fixed intensity below the intensity regime where nonlinear photoabsorption becomes relevant. Thus, the appearance of low kinetic energy fragments and, consequently a shift of the curve's center of gravity towards smaller energies is not a specific high intensity nonlinear effect.

In Fig. 3(b) energy distributions calculated under the same conditions as in Fig. 3(a), but now using LIP are depicted. Up to an intensity of approximately 10^{11} W/cm^2 the spectra are nearly identical with the ones obtained from FGR. At 10^{12} W/cm^2, however, more fragments originating from low vibrational states appear than predicted by FGR. This effect becomes more dramatic when essentially only low vibrational states are populated (not shown in Fig. 3).

In addition to the appearance of fragments with low kinetic energy, FGR also predicts the broadening of the angular distribution of photofragments with increasing laser intensity *and/or* interaction time. For the parallel transition $A\,{}^2\Sigma_u^+ \rightarrow D\,{}^2\Sigma_g^+$ in $\mathrm{Ar_2}^+$, or ${}^2\Sigma_g^+ \rightarrow {}^2\Sigma_u^+$ in $\mathrm{H_2}^+$, a distribution proportional to $\cos^2(\theta)$ is expected at low laser intensity. For increasing laser intensity, the dissociation from molecules whose dipole moments make a small angle θ with the axis of laser polarization saturates and the appearance of relatively more fragments at larger angles is expected. This has been confirmed experimentally for $\mathrm{Ar_2}^+$ at different (low) laser intensities (Sec. IV A [34]). The strongly nonlinear behavior of the dissociation rates for low vibrational states at high intensity (Fig. 2 [26]) favors the dissociation of molecules with their dipole moment aligned along the axis of laser polarization. This leads to the opposite effect, that is, a narrowing of the angular distribution at high intensity. Alignment of molecules prior to dissociation, in addition, may lead to a narrower distribution of photofragments. This alignment may be rationalized in terms of LIP: The angle-dependent deformation of the lower adiabatic potential E_1 [compare Eq. (11)], and consequently the lowering of the adiabatic vibrational states as compared to the diabatic ones creates a θ-dependent potential and the molecules tend to minimize their energy in the laser field by alignment with the laser polarization.

III. EXPERIMENTAL SETUP

$\mathrm{Ar_2}^+$ molecules are generated in a dc-discharge, accelerated to a kinetic energy $U_0 = 7.5$ keV, mass selected, and formed into a well collimated beam. A strongly focussed pulsed dye laser beam crosses the molecular beam at right angle and generates charged (Ar^+ ions) and neutral (Ar atoms) photofragments to be counted by a secondary electron multiplier and a multichannel detector, respectively. The latter provides a two-dimensional projection of the three-dimensional momentum distribution of the neutral fragments. For some experiments an additional pulsed Nd:YAG laser is used to depopulate certain rovibrational states before the interaction with the high intensity dye laser takes place. Each of these major elements of the setup is described in more detail in what follows.

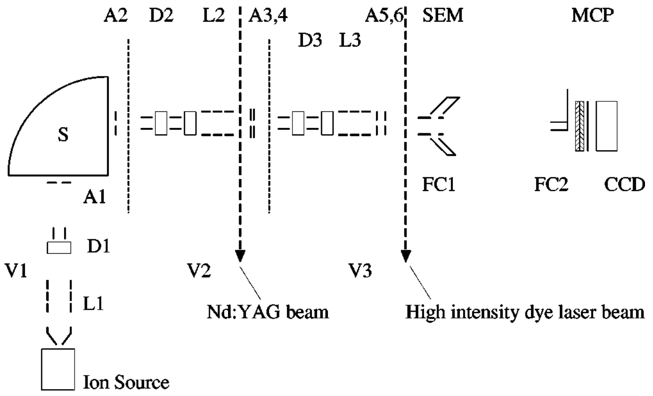

FIG. 4. Schematic drawing of molecular beam apparatus (not drawn to scale). Ion Einzel lenses are indicated by the letter *L*; deflection plates, *D*; apertures, *A*; sector magnet, *S*; secondary electron multiplier, SEM; Faraday cup, *F*; Multichannel plates, MCP; charge coupled device (camera), CCD; differentially pumped vacuum chamber, *V*.

A. Ion beam apparatus

An ion source of the duoplasmatron type [38] was used to generate $\mathrm{Ar_2}^+$ molecules in the ground state $A\,^2\Sigma_u^+$ via three body collisions

$$\mathrm{Ar}^+ + \mathrm{Ar} + \mathrm{Ar} \rightarrow \mathrm{Ar_2}^+ + \mathrm{Ar}.$$

Since the vibrational and rotational energy level spacing of $\mathrm{Ar_2}^+$ is much smaller than the average translational energy of ions in the discharge, energy exchange between translational and internal degrees of freedom is very efficient, and a thermal distribution of the populations of rovibrational states is expected [39,40]. This was confirmed by measurements of the photodissociation cross section over a wide range of wavelengths which depends sensitively on the rovibrational populations [34]. Molecules in excited electronic states that are possibly created in the discharge do not reach the interaction zone with the high intensity dye laser [40].

The ion source is held on a positive potential of 7.5 kV relative to the rest of the apparatus to extract ions from the source and accelerate them (Fig. 4). An Einzel lens and electrostatic deflection plates are used to steer the beam through the entrance slit of a sector magnet that is set (by choosing the appropriate current through the magnet coils) to transmit only $(^{40}\mathrm{Ar}^{40}\mathrm{Ar})^+$ molecules. Two more sets of electrostatic lenses and deflection plates serve to align the molecular beam along the axis given by apertures $A5$ and $A6$ and the removable Faraday cup 2 positioned immediately before the multichannel plate (MCP) detector at the end of the beam line (lens $L3$ was not used for the experiments reported here). Aperture $A4$ has a diameter of 1.5 mm and is separated from $A5$ by ≈ 40 cm. Apertures $A5$ and $A6$ (diameter ≈ 0.5 mm for the experiments reported here, in previous experiments [25] it was ≈ 1 mm) are spaced apart 12 cm. The molecular beam path between Faraday cup 1 and MCP detector is shielded against electric and magnetic stray fields using cylinders of copper and of high-permeability metal, respectively. A focussed dye laser beam crosses the molecular beam 1.5 cm behind $A6$ (interaction zone) where charged (Ar^+) and neutral (Ar) photofragments are generated. Ar^+ ions are deflected into the secondary electron multiplier (channeltron) while Ar atoms continue to travel towards the MCP detector separated from the interaction zone by 0.87 m.

Two orthogonal stainless steel wires of 28 μm diameter can be moved across the molecular beam and serve to measure its transverse density profile $f(y,z)$ in the interaction zone. The density distribution is radially symmetric when the beam is properly adjusted and one finds

$$f(\rho = \sqrt{y^2 + z^2}) = -\alpha\rho^2 + \beta \quad \forall \rho \leqslant \rho_0. \tag{15}$$

The parameters α and β are fixed by $\alpha = 2n/\pi\rho_0^4$ and $\beta = 2n/\pi\rho_0^2$, where ρ_0 is the beam radius, $n = J/e$ the number of molecules passing through the beam cross section per second, J the measured beam current, and e the elementary charge. For the high intensity data reported below J is measured to be 3.0 nA.

In order to reduce spatial averaging over the intensity distribution in the focal region of the laser beam, the radius of the molecular beam, ρ_0 of Eq. (15) beam has been reduced to 0.3 mm (compared to 0.7 mm in previous experiments [25]) by replacing the apertures $A4$ and $A5$ shown in Fig. 4. Then the molecular beam current at the laser interaction zone was again maximized by properly adjusting the voltages on all deflection plates and ion lenses. Also the ion source parameters (in particular the pressure) were modified as to maximize again the beam current at the interaction zone.

B. Detection of photofragments

Ionic photofragments are deflected towards a secondary electron multiplier where every fragment creates a current pulse that is amplified and fed into a counter. In addition to measuring the number of photofragments as a function of intensity and wavelength of the laser light, important information can be obtained from the analysis of the energy and angular distributions of the fragments. The method used here makes it possible that each photofragment contributes to the measurement of these distributions without the necessity of scanning an energy analyzer or of varying the relative angle between laser polarization and detection direction. The fact that neutral fragments are detected makes the method insensitive to stray or patch fields.

Neutral photofragments impinge on two stacked multichannel plates of 40 mm diameter (Chevron type) at the exit of which a localized electron avalanche is created. The electrons are accelerated towards a phosphor screen where a light spot appears for each fragment. The phosphor screen in turn is coupled via fiber optic taper to a cooled CCD chip providing an image of the two-dimensional detected distribution of photofragments.

The interaction zone between the tightly focused laser beam and the molecular beam is in this experiment to good approximation a point source for photofragments. In the center of mass frame of the initial $\mathrm{Ar_2}^+$ molecules, fragments having gained velocity v during the photodissociation process are found on the surface of a sphere at any given time t after dissociation. While the center of mass moves in the

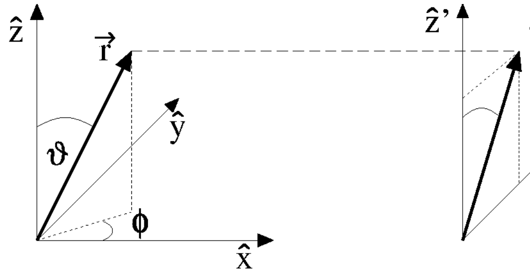

FIG. 5. The origin of the laboratory frame is taken in the center of the laser beam focus. The molecular beam travels in the *x* direction and the laser beam propagates in the *y* direction having its polarization along the *z* axis. Photofragments appear in the lab frame under the polar angles ϑ and ϕ. The distance a fragment has travelled in the molecular frame between the time of dissociation and time of arrival at the detector is indicated by the length of $\vec{r}$. The primed coordinate system has its origin in the center of the MCP detector.

laboratory frame towards the MCP detector at velocity $v_0 = \sqrt{U_0/m_{\mathrm{Ar}}}$, this sphere expands between $t=0$ (time of dissociation) and $t=t_0$ (time of arrival at the detector) at a rate determined by the velocity $v=\sqrt{2U_D/m_{\mathrm{Ar}}}$ of the photofragments (here we consider homonuclear diatomics only, with kinetic energy U_D of each fragment having mass m_{Ar}). The density distribution of fragments on the surface of such a sphere corresponds to the three-dimensional momentum distribution of fragments generated in the photodissociation process. Thus, at $t=t_0$ one obtains a two-dimensional projection $G_{t_0}(y',z')$ of the three-dimensional momentum distribution $F_{t_0}(\vartheta,\phi)$ (see Fig. 5 for the definition of the coordinates). The direction of laser polarization determines an axis of symmetry (i.e., F is independent of ϕ) of the fragment density distribution that originates in the experiments described here from a so-called parallel electronic transition (the transition dipole moment is parallel to the internuclear axis). This axial symmetry makes it possible to reconstruct the full three-dimensional (3D) distribution from its projection by applying an inverse Abel transform [41].

The projection of the momentum distribution may be slightly distorted, since the time t_0 needed to travel from the interaction zone to the detector depends on the angles ϑ and ϕ under which the fragments appear in the center of mass frame $t_0=s/(v_0+v\sin\vartheta\cos\phi)$ where s is the distance between interaction zone and detector. However, here we have $v_0=1.34\times10^5$ m/s$\gg v\approx1.5\times10^3$ m/s and setting $t_0=s/v_0$ has only a marginal effect on the reconstructed momentum distribution.

The 2D projection and 3D original distribution are related by $G_s(y',z')dS_{y'z'}=F_s(\vartheta)dS_{\vartheta\phi}$ where dS_{ij} is the respective surface element. Using the above approximation a 3D distribution from a parallel molecular transition followed by immediate dissociation $[F(\vartheta)\propto\cos^2\vartheta]$ yields the 2D projection

$$G_s(y',z')=\frac{3}{4\pi}\frac{1}{r_{\max}^3}\frac{z'^2}{\sqrt{r_{\max}^2-z'^2-y'^2}}, \tag{16}$$

where $r_{\max}\equiv sv/v_0$. In a real experiment we will not have an ideal point source for photofragments, instead this image will be convoluted with the initial distribution of fragments in the interaction zone between laser and molecular beam.

The maximum energy, $U_D^{\max}$ a photofragment may have, in order to be registered by the MCP system is given by

$$U_D^{\max}=\frac{1}{2}\left(\frac{z'_{\max}}{s}\right)^2U_0, \tag{17}$$

where $2z'_{\max}\approx32$ mm is the extension of the MCPs imaged onto the CCD chip in the z' direction, and we get $U_D^{\max}\approx1.3$ eV. The relative energy resolution

$$\delta U_D/U_D^{\max}=[2p\,\delta p+(\delta p)^2]/p_{\max}^2 \tag{18}$$

of the image of the fragment distribution varies with the momentum p a photofragment gained in the photodissociation process. The relative momentum resolution $\delta p/p_{\max}$ in turn is determined by the spatial resolution of the MCP system which yields $\delta p/p_{\max}=0.01$. These results are valid for a perfectly collimated molecular beam. However, its divergence of about 2 mrad (full angle) limits the relative energy resolution to values between 0.001 and 0.06 which gives $\delta U_D=1.3$ meV in the center region of the image and $\delta U_D=80$ meV at the edges.

Brehm *et al.* [43] showed that the detection efficiency η_{MCP} of the microchannel plates used in this experiment is 0.43 for Ar ions at 3.75 keV kinetic energy. Even though the mode of reading out the MCPs is different in the present study, the overall detection efficiency remains the same [40].

The overall efficiency η_{Ch} of the channeltron detection chain (including ion optics and electronic processing) can be determined by comparing the number of events counted by the channeltron and the MCPs. Compared to previous experiments [25] η_{Ch} was improved by changes in the geometry of the deflection plates.

C. Laser

A commercial, modified dye laser (Lambda Physik LPD 3000) pumped by a XeCl laser (Lambda Physik LPX 200) delivers 30-ns pulses of up to 15 mJ energy per pulse and is operated at a repetition rate of 15 Hz. Since a complete quantitative description of the results of photodissociation experiments is desired, much effort had to be devoted to improve and determine the exact emission characteristics of this dye laser.

The linearly polarized dye laser beam is focused onto the molecular beam using a laser monochromat optimized for diffraction limited focussing (focal length $f=20$ mm and aperture $D=4.5$ mm). A CCD camera served to measure the transverse intensity distribution of the unfocused laser beam which is well described by Gaussian curves with slightly different beam waists in the x and z directions, respectively. In order to test the beam quality in the focal region, the laser focus was imaged onto the CCD camera (imaging ratio 1:97). The result of such a measurement of a single laser pulse is shown in Fig. 6. The insets in Fig. 6 depict a cut

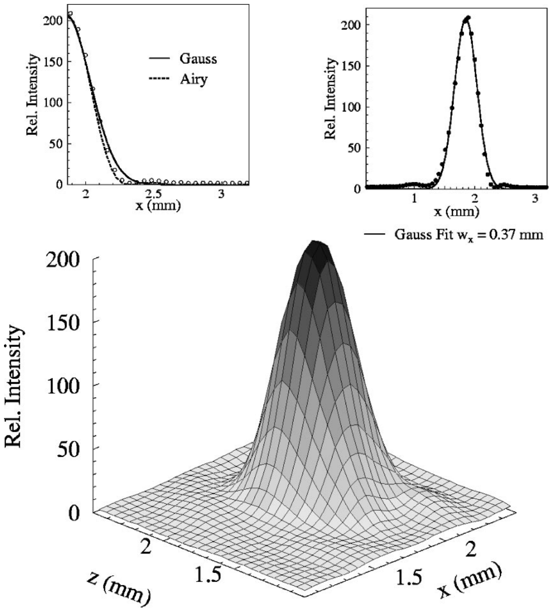

FIG. 6. Transverse intensity distribution of a single laser pulse in the center of the laser focus imaged onto a CCD camera (imaging ratio 1/97). The inset on the upper right shows a cut ($z=$const) through the intensity maximum and a Gauss fit of the measured data. The left inset shows in addition the calculated intensity distribution (labeled ''Airy'') taking into account diffraction at the finite aperture of the focussing lens.

along the straight line $z=$const (same coordinates as in Fig. 5) through the maximum of laser intensity together with a Gaussian fit and the calculated intensity distribution. The fit using $I(x,z)=I_0(z=0)\exp[-2x^2/w_x(0)^2]$ gives $w_x(z=0)=0.37/97=3.8$ μm, whereas the calculated value for the waist is 3.7 μm assuming propagation without diffraction. A more realistic calculation [42] takes into account diffraction at the aperture of the focussing lens. The dashed line in the left inset of Fig. 6 shows the result of such a calculation (at the lens $w_x=0.90$ mm, wavelength $\lambda=513$ nm) to be compared with the Gaussian fit.

It can be shown (compare Ref. [42]) that diffraction at the finite aperture of the lens leads to an intensity distribution in the focal region in propagation direction ($\hat{y}$ direction) of the laser beam described by

$$I_0(y)=I_0(0)\left(\frac{\sin(uy)}{uy}\right)^2 \tag{19}$$

with

$$u\equiv\frac{2\pi}{\lambda}\left(\frac{D}{2f}\right)^2\frac{1}{8}, \tag{20}$$

where $y=0$ lies in the center of the focus. When simulating the experiment numerically, a transverse Gaussian intensity distribution (obtained from a fit to the measured distribution) and expression (19) for the distribution in the y direction have been used: $I(x,y,z)=I_0(y)\times\exp[-2x^2/w_x(y)^2-2z^2/w_z(y)^2]$. The high intensity data given in Sec. IV B were taken with a focused laser beam characterized by $w_x(0)=2.6$ μm and $w_z(0)=2.3$ μm (wavelength 532 nm).

Meaningful experimental photodissociation data requires averaging over a large number of laser pulses. The repeatability of laser beam parameters is thus of importance. Variations in laser beam parameters have been evaluated by recording the transverse intensity profile of many laser pulses and fitting each of them with a Gaussian envelope. The variation in laser pulse energy (measured using a calibrated, NIST-traceable pyroelectric detector) and beam diameter from pulse to pulse is below 3% (standard deviation). At the location of the focussing lens, the intensity distribution had its peak value within ± 0.1 mm.

The temporal intensity profile of the dye laser pulses depends mainly on the operating parameters of the excimer pump laser (discharge voltage, repetition rate). For each experimental run the temporal intensity profile is recorded using avalanche photodiodes in connection with a fast digitizing oscilloscope (sampling rate 1 GHz). The spatial laser beam profile, too, is constantly monitored during data taking.

The transit time of molecules through the focus of the laser beam is much shorter than the dye laser pulse length. Thus, the length, $2t_0(y)=2w_x(y)/v$ and temporal shape, $I_M(t)$ of the laser pulses experienced by the molecules depend to very good approximation only on their velocity v and the spatial intensity distribution in the focus of the laser beam. Using $v=1.34\times10^5$ m/s, $w_x=2.6$ μm, and the intensity distribution given above, we obtain $2t_0(y)\geqslant 38.8$ ps and $I_M(t)=I_M^0(y,z)\exp(-2t^2/t_0)$ where $I_M^0(y,z)\equiv I_0(y)\exp[-2z^2/w_z(y)^2]$.

For some experiments an additional pulsed Nd:YAG laser (Spectra Physics) operating at 532 nm is used to deplete certain rovibrational levels of the electronic ground state $A\,{}^2\Sigma_u^+$ before the molecules interact with the high intensity dye laser beam. The Nd:YAG beam is expanded to a diameter of $\pi w_x^Y\approx 50$ mm and then focused by a cylindrical lens ($f_Y=350$ mm) having its nonfocusing axis oriented parallel to the molecular beam. The laser beam intersects at right angle the molecular beam before apertures $A3$ and $A4$ (Fig. 4). The distance between cylindrical lens and molecular beam is adjusted such that the laser beams smaller diameter $\pi w_z^Y=1.6$ mm, which is about the same as the diameter of the molecular beam (1.5 mm) where both intersect. For the experiments described below, laser pulses having a FWHM of 6 ns and average energy 38 mJ at the location of the molecular beam were used. Exact timing between pulses of the Nd:YAG laser and the dye laser (and the electronics used for detection of the photofragments) is achieved by using avalanche photodiodes for detection of the laser beams and precise delay and pulse generators. The time delay between Nd:YAG laser pulse and dye laser pulse is adjusted such that molecules that interacted with the Nd:YAG laser beam in its center (in the x direction) then interact with the focused dye laser.

D. Simulation of the experiment

The simulation of the photodissociation experiment, i.e., the calculation of the number of photofragments from a given vibrational level under laser irradiation proceeds as follows: the energy eigenvalue of this vibrational level for a given rotational quantum number is obtained by numerically integrating the time independent Schrödinger equation for the $A\,^2\Sigma_u^+$ state. Then, the dissociation rate for this level is calculated as a function of laser intensity using either LIP or FGR. The rate is plugged into a differential equation for the number of molecules present in the laser field

$$dN_{\omega_L,\nu,K}(t)=-N_{\omega_L,\nu,K}(t)R_{\omega_L,\nu,K}(I(t),\theta)dt. \tag{21}$$

After replacing dt by $(1/v)dx$ (the molecular beam travels in the x direction with velocity v) Eq. (21) is integrated over spatial coordinates and solid angle:

$$N_{\omega_L,\nu,K}=\frac{1}{\pi}\int_0^{\rho_0}\int_0^{2.3w(y)}\int_0^{\pi}N^0_{\nu,K}(y,z)\times\exp\left(\frac{1}{v}\int_{-2.3w(y)}^{2.3w(y)}R(x,y,z,\theta)dx\right)\sin\theta d\theta dz dy. \tag{22}$$

The dissociation rate R is intensity dependent and thus depends on the location of a molecule in the focal region of the laser beam. Furthermore, an integration over the temporal profile of the laser pulse has to be carried out. Integration limits have been chosen to include 99.99% of laser intensity. The number of molecules per unit area in rovibrational state with quantum numbers ν and K that pass through the laser beam during one laser pulse with length t_L is given by

$$N^0_{\nu,K}(y,z)=f(\rho=\sqrt{y^2+z^2})t_L\frac{1}{Z}\sum_{\nu,K}(2K+1)e^{-(D_e-U_{\nu,K})/kT} \tag{23}$$

with dissociation energy D_e of the $A\,^2\Sigma_u^+$ state, Boltzmann constant k, temperature T, and Z is the partition function.

For the laser pulses used in this experiment ($\geqslant 39$ ps FWHM), the energy eigenvalues of the vibrational levels follow adiabatically the change in shape of the lower LIP E_1, i.e., the initial diabatic vibrational level ends up as a single adiabatic level of E_1 once the intensity has reached its peak value (other vibrational levels are not populated during the turning on and off of the laser pulse). This is the case, as long as the relative change in intensity $|(dI/dt)/I|$ is much smaller than $1/\tau$, which is always true for the laser pulses employed in this experiment. Also, the shift in energy of adiabatic levels compared to diabatic levels at the peak intensity in the lower LIP E_1 is small. Even though the dissociation rate of a particular ν,K level at certain intensities may be changed by such a shift in energy, the result of the numerical simulation (after averaging over many states) is not affected visibly, and the conclusions drawn from this simulation are not altered. By inspection of Fig. 2 one notices that the deformation of E_1, and consequently the shift of low vibrational levels is small in the intensity range of this experiment (as is customary, experimental peak intensities are given for the data discussed in Sec. IV B. Most of the molecules experience, however, a lower intensity in the focal region).

Some experiments require the use of an additional laser to depopulate high vibrational states. This laser beam is not focused in the x direction and only weakly focused in the z direction at the location of the molecular beam, so that its variation in intensity in the x and y directions over the range of the molecular beam can be neglected. Starting with a similar differential equation as Eq. (21) and integrating over the time the laser pulse of energy E is on, we get

$$\Delta N_{\nu,K}=\frac{1}{\pi}\int_{\cos\theta_2}^{\cos\theta_1}du\int_{-z_0}^{z_0}dz N(z)\times\exp\left(-3\sigma_{\nu,K}u^2\frac{\lambda}{hc}\frac{2E}{w_z^Y w_y^Y}e^{-2(z/w_z^Y)^2}\right). \tag{24}$$

For a given rovibrational state the fraction $\Delta N_{\nu,K}$ $(0\leqslant\Delta N_{\nu,K}\leqslant 1)$ of its original population in the interval $[\theta_1,\theta_2]$ remains and interacts with the high intensity laser beam further down the molecular beam line. The y- and z-dependent distribution of molecules has been integrated over y and normalized to obtain

$$N(z)=\frac{8}{3}\frac{1}{\pi z_0^4}(z_0^2-z^2)^{3/2}\quad\forall z<z_0=\rho_0.$$

IV. EXPERIMENTAL RESULTS

A. Results at low laser intensity

For the interpretation of experimental results in intense laser fields it is necessary to know (i) which of the four lowest electronic states [32] of Ar_2^+ interact with laser light at 532 nm, (ii) the potential curves of the relevant electronic states, (iii) the magnitude of the electronic transition dipole moment $\mu(r)$, and (iv) the occupation probability of rovibrational levels of the electronic ground state $A\,^2\Sigma_u^+$. Photodissociation studies at low laser intensity at various wavelengths yield all of the desired information. Some results of these studies are outlined in what follows, and a detailed account will be given elsewhere [34].

(i) Transitions induced by a light field at 532 nm from $A\,^2\Sigma_u^+$ to one of the dissociative states $B\,^2\Pi_g$ or $D\,^2\Sigma_g^+$ lead to characteristic angular distributions of photofragments. For the parallel transition $A\,^2\Sigma_u^+\rightarrow D\,^2\Sigma_g^+$ the distribution function is proportional to $\cos^2(\theta)$, whereas for the perpendicular transition $A\,^2\Sigma_u^+\rightarrow B\,^2\Pi_g$ the dissociation probability is proportional to $\sin^2(\theta)$ (θ is the angle between the direction of laser polarization and internuclear axis). A distribution of fragments due to a perpendicular transition would have its intensity maximum in the center (along the straight line $z'=0$) of the 2D detector. The $\cos^2(\theta)$ distribution from a parallel transition on the other hand, has zero intensity along this line. Thus, the respective contribution of each transition to the total photofragment yield can be clearly distinguished by measuring the angular distribution of photofragments.

Fitting the angular distribution obtained after performing an Abel-transform of the original data (not shown) recorded with an unfocused laser beam at 495 nm at a peak intensity of 2×10^4 W/cm^2 using

$$F_\beta(\vartheta)=\frac{1}{4\pi}\left(1+\frac{\beta}{2}(3\cos^2\vartheta-1)\right) \tag{25}$$

gives $\beta=1.99\pm0.02$. For immediate dissociation following a parallel molecular transition $\beta=2$ is expected. In that particular case, Eq. (25) reduces to $F_2(\vartheta)=(3/4\pi)\cos^2(\vartheta)$. For $\beta=-1$ expression (25) yields $F_{-1}(\vartheta)=(3/8\pi)\sin^2(\vartheta)$, the angular distribution of photofragments from a perpendicular transition. Increasing the laser peak intensity to 2×10^5 W/cm^2 results in a fitted value of $\beta=1.48\pm0.03$, that is, the angular distribution becomes broader at higher intensity, since the dissociation from molecules whose transition moment make a small angle with the laser polarization starts to saturate. Here, $\beta<2$ is not due to a contribution from a perpendicular transition, since at the center of the detector there are still no fragments present. (To be more precise, the number of fragments registered in the center is still at the noise level.)

These measurements show that for the relevant laser wavelength the transition $A\,^2\Sigma_u^+\rightarrow B\,^2\Pi_g$ is strongly suppressed and treating $\mathrm{Ar_2}^+$ in this study as a two-electronic state system is an excellent approximation. (ii) The energy distribution of photofragments together with results from numerous previous studies on $\mathrm{Ar_2}^+$ [35,33] provide reliable potential curves for the $A\,^2\Sigma_u^+$ and $D\,^2\Sigma_g^+$ states. (iii) and (iv) Measuring the absolute cross section for photodissociation over a range of wavelengths (485–550 nm) gives the magnitude of the transition dipole moment μ_Σ between $A\,^2\Sigma_u^+$ and $D\,^2\Sigma_g^+$ in the relevant range of internuclear separation r (the functional dependence of μ_Σ depends linearly on r as is shown in several *ab initio* calculations [33]). In addition, the rovibrational population distribution relevant for previous high intensity experiments [25] has been determined from these cross section measurements. It has been shown that the population followed a Boltzmann distribution at a temperature corresponding to $kT=0.10$ eV [34]. For the derivation of the population distribution only the relative variation of the cross section with wavelength is relevant, not its absolute value.

B. High-intensity data

Processes that could possibly interfere with an unambiguous interpretation of results of this photodissociation study are multiphoton dissociation of $\mathrm{Ar_2}^+$ and ionization of either $\mathrm{Ar_2}^+$ or of its photofragments. Multiphoton ionization would change the ratio between the number of detected charged and neutral photofragments, respectively with changing laser intensity (for ideal, i.e., $\eta=1$, detectors this ratio would equal one at low intensity). By monitoring the neutral and charged fragment yield simultaneously, it was shown that ionization does not play a role in the present experiment (Fig. 4 in Ref. [25]).

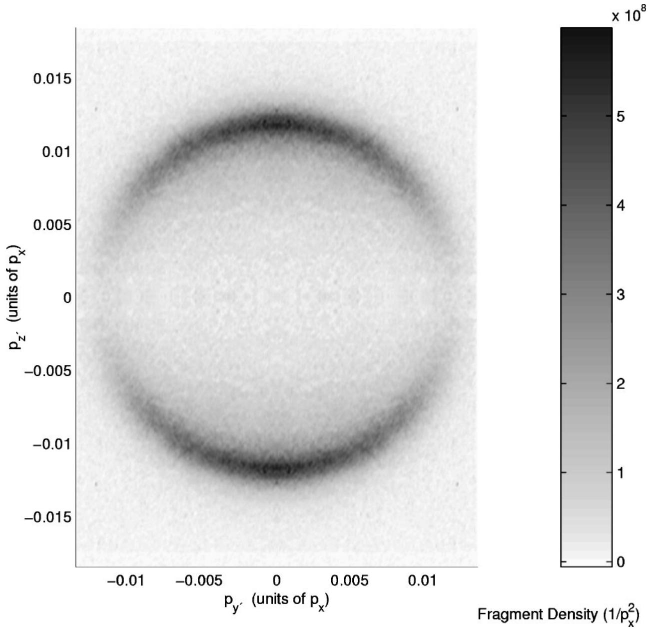

FIG. 7. Measured 2D projection of the 3D momentum distribution of neutral fragments from the photodissociation of $\mathrm{Ar_2}^+$ at the laser wavelength 532 nm and peak intensity 5.1×10^{12} W/cm^2. $p_{y'}$ and $p_{z'}$ indicate the projection of the original fragment momentum on the y' and z' axes, respectively, in units of $p_x=\sqrt{m_{Ar}U_0}$, the momentum of the fragments perpendicular to the detector surface.

The number of photofragments originating from multiphoton dissociation is negligible compared to the number of molecules having absorbed one net photon. This is determined by measuring the momentum distribution of neutral photofragments. Figure 7 shows the two-dimensional projection of the momentum distribution of neutral fragments at peak laser intensity 5.1×10^{12} W/cm^2. Since the image is symmetric with respect to the axes $z'=0$ and $y'=0$, the signal-to-noise ratio may be improved by folding the image first along the straight line $z'=0$, then along $y'=0$, and finally unfold it again, that is, adding up the four quadrants in the prescribed way and then dividing by 4. This operation yields the image shown in Fig. 7.

Higher order dissociation would lead to the appearance of higher energy fragments which are not observed in the experiment. The molecular beam velocity that determines how far fragments of a given kinetic dissociation energy can travel in the y' and z' directions before they hit the detector, and the distance, s between interaction zone and detector are adjusted such that the detector surface is optimally filled, i.e., fragments with kinetic energy from one-photon dissociation travel up to the edge of the detector in the y' direction. This ensures high-energy resolution (compare Sec. III B) for one-photon dissociation. If dissociation after the net absorption of more than one photon would take place, then the main peak of photofragments, for instance, from two-photon dissociation would lie close to the edge (z' direction) beyond the detector. Fragments from molecules with $|\theta|<\pi/2$ would, however, be visible on the detector, and, since the dissociation probability increases with θ, the detected number of fragments would increase towards the edge of the detector.

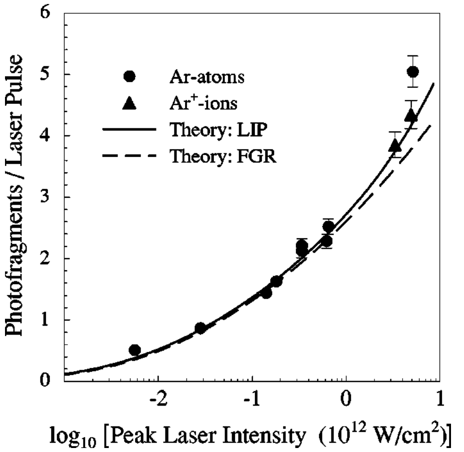

FIG. 8. Total number of photofragments registered by the MCP detector (integrated over angle and energy, averaged over 15 000 laser pulses per data point, indicated by circles) and the secondary electron multiplier (triangles) after irradiating $\mathrm{Ar}_2{}^+$ with laser light at 532 nm. The rovibrational population of the molecules is Boltzmann distributed at $kT = 0.068$ eV. The solid line shows the result of a numerical simulation of the experiment using light-induced potentials to calculate dissociation rates of $\mathrm{Ar}_2{}^+$. The dashed line is the result of a simulation using Fermi's golden rule.

Such an increase is not observed, on the contrary, the number of detected photofragments goes to zero towards the edge of the detector, and we conclude that two- and three-photon absorption are not relevant in the intensity regime studied here. These experimental findings are consistent with calculations (solving the time-dependent Schrödinger equation for $\mathrm{Ar}_2{}^+$ in ps laser pulses) by Schwendner, Seyl, and Schinke [31].

The further analysis of the measured momentum distribution requires to perform a numerical Abel transform of the experimental data. This transform is rather sensitive to noise present in the original data and results obtained from the present data do not yet yield reliable information on details of the energy and angular distribution at high laser intensity. The data taken at low laser intensity have a signal-to-noise ratio which is by about a factor 10 better than for the high-intensity data. At low intensity the laser beam is not focused and the complete molecular beam is illuminated, whereas at high intensity the tightly focused laser beam reaches only a small fraction of molecules in the beam. In future experiments a better signal-to-noise ratio for the momentum distribution data is desirable (which is most easily achieved by using a laser capable of delivering pulses of higher energy). In what follows, we shall concentrate on the total yield of photofragments, integrated over energy and angle, as a function of laser intensity.

The total number of neutral photofragments per laser pulse registered by the MCP detector at 532 nm is shown in Fig. 8 (circles). Also shown are the number of ionic fragments (Ar^+) registered by the secondary electron multiplier (triangles). The latter data points have been scaled by a factor $\eta_{\mathrm{MCP}}/\eta_{\mathrm{Ch}} = 0.43/1.16\times10^{-2}$, in order to display the two data sets from detectors with different detection efficiencies in the same graph.

The solid line represents a simulation of the experiment using LIP with experimentally determined parameters. The population of rovibrational states is Boltzmann distributed at a temperature corresponding to $kT = 0.068$ eV. Laser and molecular beam profiles are as described in Sec. III. The dashed line shows the result of a simulation using FGR which only slightly underestimates the experimental data.

Changes in the operating parameters of the ion source compared to previous experiments, make it necessary anew to determine the rovibrational temperature of the molecular ions. Previously [25,34], this has been achieved by measuring the variation of the cross section for photodissociation with laser wavelength at low laser intensity. Now, we simulate directly the high-intensity experiment and adjust the temperature T to be in accordance with detection efficiency η_{MCP}: The number of photofragments at a given laser intensity and wavelength depends sensitively on the Boltzmann-distributed population of rovibrational states and, thus, varies strongly with temperature. Therefore, the correct temperature has been determined, when the simulated curve scaled with detection efficiency $\eta_{\mathrm{MCP}} = 0.43$ coincides with one arbitrarily chosen reference data point at laser intensity I_i. Alternatively, all m data points may be taken into account by determining the minimum of the variance

$$V_T = \frac{1}{m}\sum_{i=1}^{m}\left[N^{\exp}(I_i) - \eta_{MCP} N_T^{\mathrm{theory}}(I_i)\right]^2 \qquad (26)$$

as a function of T. This was done here. The experimentally determined number of neutral fragments (circles in Fig. 8) at laser intensity I_i is denoted by $N^{\exp}(I_i)$, and $N_T^{\mathrm{theory}}(I_i)$ indicates the simulated number at this intensity for temperature T. Extracting T from the present data on the basis of the simulation with FGR leads almost to the same result. However, a detection efficiency $\eta_{\mathrm{Ch}} = 1.25\times10^{-2}$ would be required for the simulation to also be consistent with the data registered by the secondary electron multiplier.

The data in Fig. 8 agree well with the predictions of LIP, whereas FGR underestimates the number of fragments produced at laser intensities above 10^{12} W/cm^2. However, there is only a small deviation in the predictions of the two theoretical concepts.

In the FGR picture, the yield of photofragments for a given vibrational state at given laser intensity is proportional (as long as it does not saturate) to the dissociation cross section times the relative population of this state. The cross section in turn is mainly determined by the overlap integral M [Eq. (2)] which is largest for levels around the crossing point of the diabatic curves in Fig. 1. If LIP are considered, then, too, the main contribution to photodissociation is expected from just these levels in the vicinity of the avoided crossing (Sec. II C). Thus, for rovibrational distributions of the molecular population where mainly these levels contribute to the photodissociation signal, FGR and LIP lead to predictions that are not easily discernible experimentally [see also Fig. 3(a) of Ref. [26]]. Averaging over the intensity distribution in the laser focus, in addition, will diminish the effect of tunneling on the total signal.

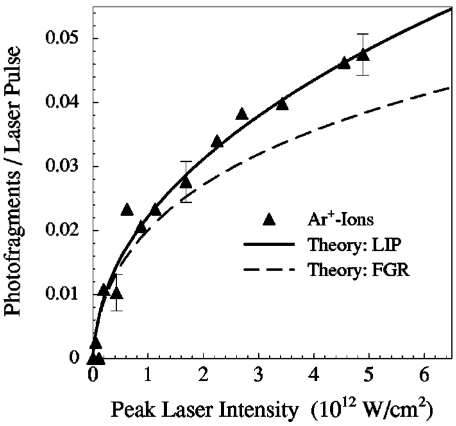

FIG. 9. Number of photofragments registered by the secondary electron multiplier (averaged over 16 000 laser pulses) as function of laser intensity after irradiating $Ar_2{}^+$ with laser light at 532 nm. An additional laser was used to depopulate high vibrational states ($\nu \geqslant 5$) before the interaction with the high-intensity laser. The solid line again is the result of a numerical simulation of the experiment using light-induced potentials, and the dashed line results from a simulation using Fermi's golden rule. The effect of tunneling of low vibrational states through a light-induced potential barrier is clearly visible.

Both, averaging over the thermal rovibrational distribution of the molecular population and over the spatial intensity distribution of the strongly focused laser beam tend to cover up new nonlinear effects in strong laser fields. In order to clearly identify tunnel dissociation predicted by LIP, it is advantageous to have only vibrational states below the diabatic crossing populated. The predictions for the dissociation rates of FGR and LIP differ by orders of magnitude for these levels, and even after averaging over the intensity distribution in the laser focus a clear difference in predictions remains [Fig. 3(b) in Ref. [26]].

For a further series of experiments an additional Nd:YAG laser at 532 nm is used to depopulate high vibrational states before the molecules reach the interaction zone with the tightly focused high intensity laser beam tuned also to the wavelength 532 nm (Secs. III D and III C). These investigations concentrated on intensities above 10^{11} W/cm^2. The number of ionic photofragments detected by the secondary electron multiplier as a function of laser intensity is shown in Fig. 9. Again, the solid line represents a simulation of the experiment using LIP and the dashed line shows the result of a simulation starting from FGR. Here, we find a distinctive difference in the predictions of LIP and FGR, respectively. At high intensity, the experimental data deviates more and more from the FGR curve, is, however, in good agreement with the simulation using LIP. FGR predicts for low vibrational states small dissociation rates, whereas in the LIP picture molecules in low ν states may tunnel through the light-induced potential barrier the easier the higher the laser intensity becomes. At a peak intensity of, for example, 5×10^{11} W/cm^2, the lower adiabatic potential well E_1 still supports the four lowest vibrational states which, however, exhibit a large tunneling rate and thus are (quasi)bound.

The conclusion that only light-induced potentials describe the data presented here does not hinge on the exact value of the absolute detection efficiency of the secondary electron multiplier $\eta_{\mathrm{Ch}} = 1.16\times10^{-2}$. Even if it had not been determined correctly, it would not be possible to consistently describe both, the data in Figs. 8 and 9 using FGR. The best possible agreement between experimental data in Fig. 9 and the simulation using FGR would be obtained, if the simulation were scaled with a factor 1.41×10^{-2} which is at variance with $\eta_{\mathrm{Ch}} = 1.25\times10^{-2}$ determined from the data in Fig. 8 under the assumption that FGR were correct.

Even if the value for η_{MCP} used here were grossly wrong, the main results of the data analysis would not be affected. A different value of η_{MCP} implies a different value of the transition dipole moment, μ_Σ that is determined from measurements of the absolute cross section for photodissociation at various laser wavelengths and low intensity. If, for example, η_{MCP} equaled 0.23 instead of 0.43, the value for μ_Σ used here had to multiplied by a factor $\sqrt{0.43/0.23}$ (the cross section is proportional to μ_Σ^2) which would yield a value for μ_Σ close to the upper limit set by *ab initio* calculations [33]. Consequently, the temperature, T determined from the high intensity data in the way described above would be 0.090 eV. Carrying out the data analysis as before would again give only a small difference in the predictions of LIP and FGR for the data shown in Fig. 8. However, the ratio between the predictions of the two models at an intensity of 5.11×10^{12} W/cm^2 would be 1.32 under the same experimental conditions as the data of Fig. 9 was taken, that is, this ratio would be even larger than for the curves shown in this figure, and the measured data could *only* be reasonably described using LIP, even if a different value for η_{MCP} were used. (The same conclusion holds true, if η_{MCP} were greater than 0.43.)

Thus, a consistent description of low-intensity data and high intensity data with two different population distributions of rovibrational states requires the use of light induced molecular potentials. At high laser intensities, tunneling through light induced potentials leaves a clear fingerprint on the experimental data in Fig. 9.

V. CONCLUDING REMARKS

A mass selected beam of $Ar_2{}^+$ serves to study photodissociation of this simply structured molecule in intense laser fields. Only two electronic states, as in $H_2{}^+$, are relevant in the wavelength range used here. Since the vibrational frequency of $Ar_2{}^+$ is about an order of magnitude smaller than for $H_2{}^+$, nonlinear effects in photodissociation—induced by the light field coupling a bound and a repulsive state—occur already at relatively moderate light intensities where, in particular ionization is not of importance. Tunneling through a light-induced potential barrier in molecules exposed to high-intensity laser fields has been observed. Light-induced molecular potentials [(LIP) molecular dressed states] do not only give intuitive insight into processes in strong laser fields, but also provide a quantitative description of this photodissociation experiment on a diatomic molecular ion.

The quantitative comparison between experimental photodissociation yield and the prediction of LIP (that takes into account nonlinear effects) in a previous study [25] showed good agreement, too. It came as a surprise when comparing the experimental data of Ref. [25] to the predictions of Fermi's golden rule (FGR)—which is not expected to be valid at high laser intensity—to find that this theory, too, even quantitatively agrees with experimental results. Here, it is shown that not only the total yield of photofragments, but also qualitative features of their energy distribution (i.e., the appearance of low kinetic energy photofragments) is predicted by FGR and thus cannot be taken as evidence for LIP. Only a quantitative analysis of the experimental data might reveal that the observed number of low-energy photofragments necessitates a new theoretical description.

We do *not* assert that FGR—under any circumstances—is the correct theory at high laser intensities. However, when investigating the photodissociation process as a function of laser intensity, in order to experimentally diagnose LIP that might play a role *above* a certain intensity, it seems obvious to start at *low* intensities, where FGR is a valid description, and look for deviations from the predictions of FGR at higher intensities. These deviations, signatures of LIP as observed in this study are in many other photodissociation experiments too of quantitative nature, and thus, need a quantitative analysis. If experiments as testing ground for theoretical predictions are taken seriously, it obviously would not be necessary to conclude that a ''new'' theory (here LIP) is valid—even if the experimental results are consistent with this theory—if these results were explicable in terms of an ''old'' theory (here FGR). The comparison of photodissociation yields with predictions of FGR on one hand and LIP on the other should be understood in this sense. Another intriguing feature of LIP, *trapping* in a light-induced potential well and thus, stabilization against dissociation in an intense field, will be at the center of future experimental studies using this molecular beam apparatus.

ACKNOWLEDGMENTS

We gratefully acknowledge technical assistance by W. Simon, K. Linner, and H. Brückner.

[1] *Atoms in Intense Laser Fields*, edited by M. Gavrila (Academic Press, San Diego, 1992).

[2] *Molecules in Laser Fields*, edited by A. D. Bandrauk (Marcel Dekker, New York, 1994).

[3] A. M. F. Lau and C. K. Rhodes, Phys. Rev. A **16**, 2392 (1977); T. F. George, I. H. Zimmermann, J.-M. Yuan, J. R. Laing, and P. L. DeVries, Acc. Chem. Res. **10**, 449 (1977).

[4] S. Haroche, Ann. Phys. (Paris) **6**, 189 (1971); **6**, 327 (1971); C. Cohen Tannoudji, J. Dupont-Roc, and G. Grynberg, *Atom-Photon Interactions* (Wiley, New York, 1992), Chap. 6.

[5] Andre D. Bandrauk and Michael L. Sink, J. Chem. Phys. **74**, 1110 (1981).

[6] A. D. Bandrauk and M. L. Sink, Chem. Phys. Lett. **57**, 569 (1978).

[7] O. Atabek, M. Chrysos, and R. Lefebvre, Phys. Rev. A **49**, R8 (1994); E. Charron, A. Giusti-Suzor, and F. H. Mies, J. Chem. Phys. **103**, 7359 (1995).

[8] E. Charron, A. Giusti-Suzor, and F. H. Mies, Phys. Rev. Lett. **71**, 692 (1993). Here we restrict the discussion to methods using intense fields to control molecular dynamics. Another method, is, for example, control of molecular or atomic processes relying on the interference between different excitation paths, in weak fields, that lead to the same final state [see, for instance, P. Brumer and M. Shapiro, Sci. Am. **272**, 34 (1995)].

[9] B. Sheehy, B. Walker, and L. F. DiMauro, Phys. Rev. Lett. **74**, 4799 (1995); M. R. Thompson, M. K. Thomas, P. F. Taday, J. H. Posthumus, A. J. Langley, L. J. Frasinski, and K. Codling, J. Phys. B **30**, 5755 (1997).

[10] M. Y. Ivanov, D. R. Matusek, and J. S. Wright, Chem. Phys. Lett. **255**, 232 (1996); A. Vardi and M. Shapiro, Phys. Rev. A **58**, 1352 (1998).

[11] B. M. Garraway and K.-A. Suominen, Phys. Rev. Lett. **80**, 932 (1998).

[12] T. Zuo, S. Chelkowski, and A. D. Bandrauk, Phys. Rev. A **48**, 3837 (1993); M. Yu. Ivanov, P. B. Corkum, and P. Dietrich, Laser Phys. **3**, 375 (1993); A. D. Bandrauk and Hengtai Yu, Phys. Rev. A **59**, 539 (1999).

[13] A. Giusti-Suzor and F. H. Mies, Phys. Rev. Lett. **68**, 3869 (1992); Guanhua Yao and Shih-I Chu, Phys. Rev. A **48**, 485 (1993).

[14] For a review of theoretical and experimental work on $H_2{}^+$2 up to 1995 see A. Giusti-Suzor, F. H. Mies, L. F. DiMauro, E. Charron, and B. Yang, J. Phys. B **28**, 309 (1995).

[15] A. Zavriyev, P. H. Bucksbaum, J. Squier, and F. Saline, Phys. Rev. Lett. **70**, 1077 (1993); L. J. Frasinski, J. H. Posthumus, J. Plumridge, and K. Codling, *ibid.* **83**, 3625 (1999).

[16] M. Schmidt, D. Normand, and C. Cornaggia, Phys. Rev. A **50**, 5037 (1994).

[17] D. Normand and M. Schmidt, Phys. Rev. A **53**, R1958 (1996).

[18] K. Codling, L. J. Frasinski, and P. A. Hatherly, J. Phys. B **22**, L321 (1989); T. Seideman, M. Yu. Ivanov, and P. B. Corkum, Phys. Rev. Lett. **75**, 2819 (1995); T. Zuo and A. D. Bandrauk, Phys. Rev. A **52**, R2511 (1995).

[19] E. Constant, H. Stapelfeldt, and P. B. Corkum, Phys. Rev. Lett. **76**, 4140 (1996).

[20] G. N. Gibson, M. Li, C. Guo, and J. Neira, Phys. Rev. Lett. **79**, 2022 (1997).

[21] P. Dietrich, M. Yu. Ivanov, F. A. Ilkov, and P. B. Corkum, Phys. Rev. Lett. **77**, 4150 (1996); K. C. Kulander, F. H. Mies, and K. J. Schafer, Phys. Rev. A **53**, 2562 (1996); Weixing Qu, Suxing Hu, and Zhizhan Xu, *ibid.* **57**, 2219 (1998); I. Kawata, H. Kono, and Y. Fujimura, Chem. Phys. Lett. **289**, 546 (1998); T. D. G. Walsh, F. A. Ilkov, S. L. Chin, F. Châteauneuf, T. T. Nguyen-Dang, S. Chelkowski, A. D. Bandrauk, and O. Atabek, Phys. Rev. A **58**, 3922 (1998); K. Drese and M. Holthaus, Eur. Phys. J. D **5**, 119 (1999); R. Numico, A. Keller, and O. Atabek, Phys. Rev. A **60**, 406 (1999); Sylvie Magnier, Maurizio Persico, and Naseem Rahman, Phys. Rev. Lett. **83**, 2159 (1999).

[22] P. H. Bucksbaum, A. Zavriyev, H. G. Muller, and D. W. Schu-

macher, Phys. Rev. Lett. **64**, 1883 (1990); A. Zavriyev, P. H. Bucksbaum, H. G. Muller, and D. W. Schumacher, Phys. Rev. A **42**, 5500 (1990).

[23] Sarah W. Allendorf and Abraham Szöke, Phys. Rev. A **44**, 518 (1991); B. Yang, M. Saeed, L. F. DiMauro, A. Zavriyev, and P. H. Bucksbaum, *ibid.* **44**, R1458 (1991); S. Yang and W. T. Hill III, *ibid.* **51**, 2301 (1995); F. A. Ilkov, S. Turgeon, T. D. G. Walsh, and S. L. Chin, Chem. Phys. Lett. **247**, 1 (1995); H. Rottke, J. Ludwig, and W. Sandner, Phys. Rev. A **54**, 2224 (1996); C. Trump, H. Rottke, and W. Sandner, *ibid.* **60**, 3924 (1999).

[24] V. R. Bhardwaj, F. A. Rajgara, K. Vijayalakshmi, V. Kumarappan, D. Mathur, and A. V. Sinha, Phys. Rev. A **58**, 3849 (1998); J. H. Posthumus, J. Plumridge, K. Codling, L. J. Frasinski, A. J. Langley, and P. F. Taday, Laser Phys. **9**, 163 (1999); S. Banerjee, G. Ravindra Kumar, and D. Mathur, Phys. Rev. A **60**, R25 (1999).

[25] Christof Wunderlich, Hartmut Figger, and Theodor W. Hänsch, Chem. Phys. Lett. **256**, 43 (1996).

[26] Chr. Wunderlich, E. Kobler, H. Figger, and T. W. Hänsch, Phys. Rev. Lett. **78**, 2333 (1997).

[27] Chr. Wunderlich, H. Figger, and T. W. Hänsch, in *Multiphoton Processes 1996*, edited by P. Lambropoulos and H. Walther (Institute of Physics, Bristol, 1997), p. 254.

[28] K. Sändig, H. Figger, Chr. Wunderlich, and T. W. Hänsch, in *Laser Spectroscopy XIV International Conference* (World Scientific, Singapore, 1999), p. 310.

[29] A. D. Bandrauk, E. Aubanel, J. M. Gauthier in Ref. [2], Chap. 3.

[30] A. I. Pegarkov and L. P. Rapaport, Opt. Spectrosc. **65**, 55 (1988).

[31] Peter Schwendner, Frank Seyl, and Reinhard Schinke, Chem. Phys. **217**, 233 (1997).

[32] The Π states are each split by spin-orbit coupling into a $\Pi_{3/2}$ and $\Pi_{1/2}$ state which is not of relevance here. This will be justified in a separate publication [34] devoted to the structure of $Ar_2{}^+$.

[33] For instance, T. L. Gilbert and A. C. Wahl, J. Chem. Phys. **55**, 5247 (1971); W. J. Stevens, M. Gardner, A. Karo, and P. Julienne, *ibid.* **67**, 2860 (1977); W. R. Wadt, *ibid.* **68**, 402 (1978); **73**, 3915 (1980); P. A. Christiansen, K. S. Pitzer, Y. S. Lee, J. H. Yates, W. C. Ermler, and N. W. Winter, *ibid.* **75**, 5410 (1981); H. U. Böhmer and S. D. Peyerimhoff, Z. Phys. D: At., Mol. Clusters **4**, 195 (1986); M. T. Bowers, W. E. Palke, K. Robbins, C. Roehl, and S. Walsh, Chem. Phys. Lett. **180**, 235 (1991); C. Cachoncinlle, J. M. Pouvesle, G. Durand, and F. Spiegelmann, J. Chem. Phys. **96**, 6093 (1992); F. X. Gadea, J. Savrda, and I. Paidarova, Chem. Phys. Lett. **223**, 370 (1994); Florent Xavier Gadea and Ivana Paidarova, Chem. Phys. **209**, 281 (1996).

[34] Chr. Wunderlich, H. Figger, and T. W. Hänsch (unpublished).

[35] For instance, H.-U. Mittmann and H.-P. Weise, Z. Naturforsch. A **29**, 410 (1974); Th. M. Miller, J. H. Ling, R. P. Saxon, and J. T. Moseley, Phys. Rev. A **13**, 2171 (1976); J. T. Moseley, R. P. Saxon, B. A. Huber, P. C. Cosby, R. Abouaf, and M. Tadjeddine, J. Chem. Phys. **67**, 1659 (1977); C. Y. Ng, D. J. Trevor, B. H. Mahan, and Y. T. Lee, *ibid.* **66**, 446 (1977); R. O. Hunter, J. Oldenettel, C. Howton, and M. W. Cusker (unpublished); P. M. Dehmer and J. L. Dehmer, J. Chem. Phys. **69**, 125 (1978); R. G. Keesee and A. W. Castleman, Jr., J. Phys. Chem. Ref. Data **15**, 1011 (1986); Y. Morioka, M. Ogawa, T. Matsumoto, K. Ito, K. Tanaka, and T. Hayaishi, J. Phys. B **24**, 791 (1991); T. Pradeep, B. Niu, D. A. Shirley, J. Chem. Phys. **98**, 5269 (1993); R. Signorell, F. Merkt, *ibid.* **109**, 9762 (1998).

[36] G. H. Dunn, Phys. Rev. **172**, 1 (1968).

[37] Chaoyuan Zhu and Hiroki Nakamura, J. Chem. Phys. **101**, 4855 (1994); **101**, 10 630 (1994); **108**, 7501 (1998).

[38] H. Liebl and W. W. Harrison, Int. J. Mass Spectrom. Ion Phys. **22**, 237 (1976).

[39] L. M. Biberman, V. S. Vorob'ev, and I. T. Yakubov, *Kinetics of Nonequilibrium Low-Temperature Plasmas* (Consultants Bureau, New York, 1987).

[40] Christof Wunderlich (unpublished).

[41] Benjamin J. Whitaker in *Research in Chemical Kinetics*, edited by R. G. Compton and G. Hancock (Elsevier, Amsterdam, 1993), Vol. 1, p. 307.

[42] M. Born and E. Wolf, *Principles of Optics*, 6th ed., Kapitel 8.5, 8.8 (Pergamon, New York, 1983); L. Zhang, L. J. Frasinski, and K. Codling, J. Phys. B **27**, 3427 (1994).

[43] B. Brehm, J. Grosser, T. Ruscheinski, and M. Zimmer, Meas. Sci. Technol. **6**, 953 (1995); M. Barat, J. G. Brenot, J. A. Fayeton, and Y. J. Picard, Rev. Sci. Instrum. **71**, 2050 (2000); Galileo Corp., the manufacturer of the MCPs used here, specifies a detection efficiency for neutrals and ions at kinetic energy of 3.75 keV between 0.38 and 0.75.